




## Ice front shaping by upward convective current

Ziqi Wang <sup>1</sup>, Linfeng Jiang,<sup>1</sup> Yihong Du,<sup>1</sup> Chao Sun <sup>1,2,\*</sup> and Enrico Calzavarini <sup>3,†</sup>

<sup>1</sup>Center for Combustion Energy, Key Laboratory for Thermal Science and Power Engineering of Ministry of Education, Department of Energy and Power Engineering, Tsinghua University, Beijing 100084, China

<sup>2</sup>Department of Engineering Mechanics, School of Aerospace Engineering, Tsinghua University, Beijing 100084, China

<sup>3</sup>Université de Lille, Unité de Mécanique de Lille - J. Boussinesq - UML - ULR 7512, F-59000 Lille, France



(Received 9 December 2020; accepted 25 August 2021; published 14 September 2021)

The extent and the morphology of ice forming in a differentially heated cavity filled with water are studied by means of experiments and numerical simulations. We show that the main mechanism responsible for the ice shaping is the existence of a cold upward convective current in the system. Such a current is ascribed to the peculiar equation of state of water, i.e., the nonmonotonous dependence of density with temperature. The precise form of the ice front depends on several factors, first, the temperature difference across the cell which drives the convection, and second, the wall inclination with respect to the vertical, both of which are explored here. We propose a boundary-layer model and a buoyancy-intensity model which account for the main features of the ice morphology.

DOI: [10.1103/PhysRevFluids.6.L091501](https://doi.org/10.1103/PhysRevFluids.6.L091501)

Turbulent convective flows along with the ice formation process create intriguing coupling behaviors, which have a widespread appearance in nature and a strong relevance in industrial applications [1–5]. In general, the orientation of the temperature gradient and the gravity vector are not parallel. Their angle can play an important role in determining the ice front morphology and the system heat transfer performances. Examples are the surficial icing of lakes and rivers, floating ice bodies (e.g., icebergs), ice bodies (e.g., ice shelf) extending outward from the land into waters, and solidification in energy storage technology [6–11]. For water, the coupled physics among the phase change, turbulent convection, and the density anomaly [water density reaches a maximum  $\rho_c$  at the density peak temperature  $T_c$  ( $\approx 4^\circ\text{C}$ )] bring more challenges: Gravitationally stable and unstable stratifications coexist, which can strongly affect flow structures [12–23].

In recent years, many studies have been devoted to exploring the interplay between convective flows and thermal stratification/phase transitions under different system inclinations. For penetrative convection [14], some of these have found that the inclination can induce the breakdown of fluid stratification due to the density anomaly [24–26]. Others have explored the coupling dynamics of phase change and turbulent convection using phase-change materials [27–30]. A recent work [31], in a freezing-from-above system, showed that density anomaly induced stratification has major effects on the flow structures and the resulting ice front speed and equilibrium state. However, there is still a lack of explorations of the physical mechanisms behind the whole rich ice front morphology. One may ask: How does the ice front morphology change when the system is tilted? What are the hydrodynamical mechanisms that account for the extent and the complex ice front morphology?

In this Letter, by combining experiments, numerical simulations, and theoretical modeling, we aim to systematically explore freshwater solidification and its coupling with turbulent convective

\*chaosun@tsinghua.edu.cn

†enrico.calzavarini@univ-lille.fr

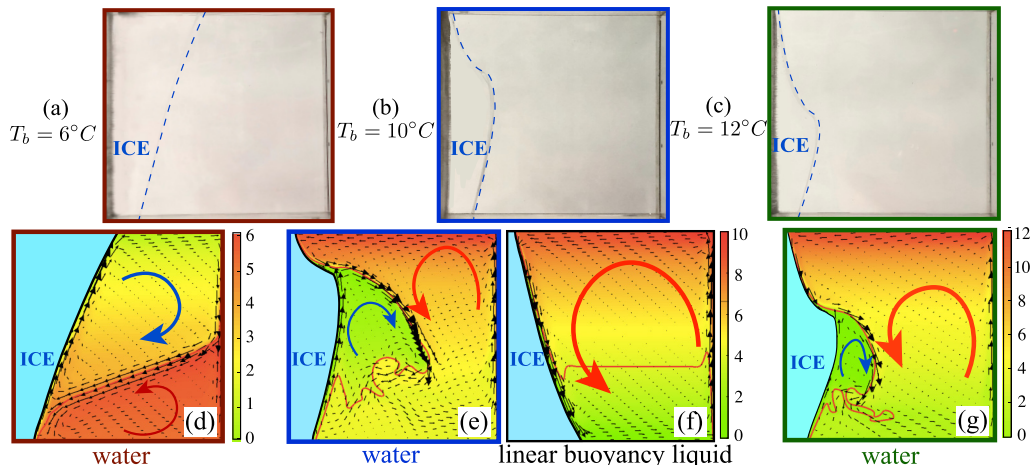


FIG. 1. Comparison of the ice morphology at the equilibrium state in VC from experiments (a)–(c), and simulations with (d), (e), (g) and without (f) considering the density anomaly. The heating condition is  $T_b = 6^\circ\text{C}$  (a), (d),  $10^\circ\text{C}$  (b), (e), (f), and  $12^\circ\text{C}$  (c), (g). (d)–(g) Temperature fields are represented in color,  $0^\circ\text{C}$  (black line) and  $4^\circ\text{C}$  (red line) isotherms, and velocity vectors (black arrows). The arrows in (d)–(g) show the large scale flow orientation in convective rolls, the blue/red colors denoting respectively the ascending cold/warm water.

flows to understand the complex behaviors of the ice front morphology at varying the system inclination angle  $\beta$  (unit: degrees). The experiments are conducted in a classical Rayleigh–Bénard (RB) convection system [32–36] (a fluid layer confined between a cold top plate, with temperature  $T_t$ , and a hot bottom plate, with temperature  $T_b$ ), with a quasi-two-dimensional rectangular shape (aspect ratios  $L_x/H = 1$  and  $L_z/H = 1/4$ , with  $H = 24$  cm in experiments). The working fluid is de-ionized ultrapure water (Prandtl number  $\text{Pr} \approx 11$ ). The simulations are performed by means of the CH4-PROJECT code [37], which adopts a lattice Boltzmann algorithm for the description of the fluid and temperature dynamics, and an enthalpy method for the ice evolution (for details, see the Supplemental Material [38]) [31,39–43]. Since the water thermal expansion coefficient inverts at  $T_c$  ( $\approx 4^\circ\text{C}$ ), here we use the nonmonotonous relationship of density with temperature for water near  $T_c$  [44],  $\rho(T) = \rho_c(1 - \alpha^*|T - T_c|^q)$ , with  $\rho_c = 999.972$  kg/m<sup>3</sup> the maximum density  $T_c \approx 4^\circ\text{C}$ ,  $\alpha^* = 9.30 \times 10^{-6}(\text{K}^{-q})$ , and  $q = 1.895$ . Both in experiments and simulations  $T_t$  is fixed at  $-10^\circ\text{C}$ . In the simulations we neglect the microscopic physics leading to kinetic undercooling, the Gibbs-Thomson effect, and the anisotropic growth/melting [45]. In this study, we monitor the local and the global ice thickness, denoted respectively  $h_i(x, t)$  and  $h_i(t)$  and expressed in units of the cell height  $H$  ( $h_i = 1$  means full solidification). We consider that the equilibrium is reached when the standard deviation of  $h_i(t)$  over a time window of about 8 min is less than 0.5%. We first show the comparison of the ice front morphology at the equilibrium state under different heating conditions (i.e. different  $T_b$ ) between experiments and simulations, under vertical convection (VC, solidification from the left with  $\beta = 90$ ). Figures 1(a)–1(c) are the experimental results with  $T_b = 6, 10,$  and  $12^\circ\text{C}$ , respectively (for more results, see the Supplemental Material [38]). The corresponding simulation results with properly considering the density anomaly are shown in Figs. 1(d), 1(e) and 1(g), representing a good agreement with the experimental measurements. This indicates that the simulation indeed can capture the correct behavior of the system. The ice front morphology displays a drastic change as  $T_b$  increases. This is due to the competition of two convective rolls originating from the density anomaly, i.e., the one originating from the plumes detaching from the hot plate [red arrow in Figs. 1(d), 1(e) and 1(g)] and the other from the cold upward convective current along the ice front [blue arrow in Figs. 1(d), 1(e) and 1(g)]. The strength of the rolls can be adjusted by

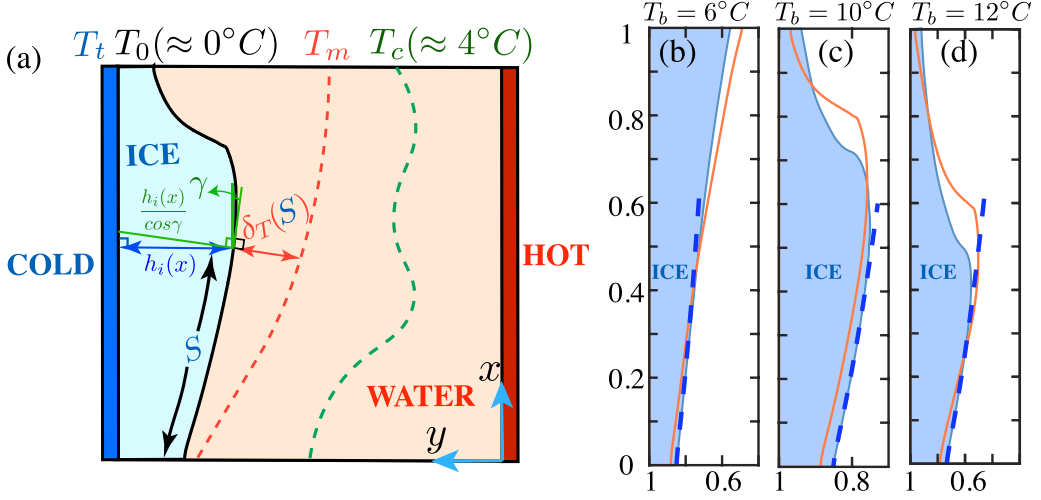


FIG. 2. Boundary-layer model to explain the ice front morphology in the VC case. (a) Sketch of the model: The ice front at  $T_0 = 0^\circ\text{C}$  (black line), the  $T_m$  isotherm which is the outer boundary of the thermal boundary (red dashed line), and the  $T_c$  isotherm (green dashed line). The angle between the tangential direction of the ice front and the  $x$  direction is  $\gamma$ ; the thickness normal to the ice front (the green thick line in the ice) is  $\frac{h_i(x)}{\cos \gamma}$  (with  $\cos \gamma = dx/dS$ ). (b)–(d) Comparison of ice front morphology among experiments (shaded area), simulations (line), and the model (dashed line) for different  $T_b$ .

changing  $T_b$ . When  $T_b = 6^\circ\text{C}$  [Fig. 1(a)], the whole ice is shielded by the upward convective current, and thus the ice front is flat but only tilted. As  $T_b$  increases to  $10^\circ\text{C}$ , the ice front becomes highly uneven and is thicker when protected by the upward convective current, thinner at the bottom, and thinnest at the top where the impingement of hot plumes increases the local heat transfer. Further, when  $T_b$  is even higher [Figs. 1(c) and 1(g)], the hot anticlockwise roll is much stronger, so it is able to intensively penetrate the cold clockwise roll and finally affect the ice front, resulting in a thinner averaged ice thickness but with a similar shape to that of  $T_b = 10^\circ\text{C}$ .

In the simulations, the flow structures and ice front profile are highly different when neglecting the density anomaly [i.e., when the density is a linear function of the temperature, see Fig. 1(f)]: There is only one convective roll, and the ice front is flat and thinner at the top and thicker at the bottom. The clear distinction between the simulation with [Fig. 1(e)] and without [Fig. 1(f)] considering the density anomaly indicates that this property is crucial to properly describe the ice formation in the presence of natural convection.

To better understand the morphology of the ice front at its steady state, we introduce a simple model based on the idea that a developing thermal boundary layer forms along the ice-water interface. We note that when the ice has ceased to grow there exists a local balance between the heat flux across the ice and the one across the boundary layer adjacent to the ice. The intensity of such fluxes can be estimated by considering the thermal difference across the ice and the boundary layer and the specific geometry of the problem, as shown in the sketch in Fig. 2(a). We introduce a curvilinear coordinate  $S$  measuring the length of the ice front starting from its boundary point at the  $x = 0$  position, which is linked to the local ice thickness by the arclength formula  $S(x) = \int_0^x \sqrt{1 + \left[\frac{d(h_i(\xi))}{d\xi}\right]^2} d\xi$ . We now express heat flux balance in the direction normal to the ice surface as

$$k_i \frac{(T_0 - T_i)}{h_i(x) \frac{dS(x)}{dx}} = k_w \frac{(T_m - T_0)}{\delta_T[S(x)]}, \quad (1)$$

where  $k_w$  and  $k_i$  are the thermal conductivity of water and ice,  $(T_0 - T_i)$  is the temperature difference in the ice, and  $h_i(x) \frac{dS(x)}{dx}$  is the ice thickness in the direction normal to the ice front. The estimation of the heat flux in the water involves making further assumptions. First, we consider that the heat transport in the boundary layer in the direction normal to the ice front is purely conductive, and this is justified by the fact that for  $\text{Pr} \gg 1$  the thermal boundary layer is nested inside the viscous one [46]. Second, we assume that the thermal difference across the fluid boundary layer is half of the one in the adjacent recirculation region [denoted with the blue arrow in Figs. 1(d), 1(e) and 1(g)], i.e.,  $(T_m - T_0)$ , with  $T_m = (T_0 + T_c)/2$ . Third, the boundary-layer thickness  $\delta_T(S)$  is assumed to vary along the ice front, as in a developing vertical thermal boundary layer, with a dependence that we take to be  $\delta_T(S) = C_1(S + C_2)^{1/4}$  [47–49]. The latter expression has two dimensionless parameters  $C_1 = c \cdot \{g[1 - \rho(T_m)/\rho_c]/(\nu\kappa)\}^{1/4}$  with  $c$  the proportional constant ( $c \approx 5 \text{ m}^{3/4}$ , and  $c$  has the unit  $\text{m}^{3/4}$  to make  $C_1$  dimensionless) [47–49], and the offset  $C_2$  because of the nonzero boundary-layer thickness at  $x = 0$ , with  $C_2 = \{h_i(0)[k_w(T_m - T_0)]/[k_i(T_0 - T_i)]/C_1\}^{1/4}$ , with the boundary ice thickness  $h_i(0)$  as an input from the simulation results. Since the sidewall is adiabatic,  $\frac{dh_i}{dx}|_{x=0} = 0$  is an extra known condition. With the above choices Eq. (1) becomes an integrodifferential equation that can be solved numerically for the local ice thickness  $h_i(x)$ . Figures 2(b)–2(d) show the comparison of the model prediction with experiments and simulations. A good qualitative agreement is reached in the region where the upward convective current takes place. The disagreement in the upper part of the ice front is expected as the boundary layer no longer develops in that region due to the downward warmer convective current [denoted with the red arrow in Figs. 1(d), 1(e) and 1(g)]. Although the exact spatial dependence of  $\delta_T$  along the ice interface is not known, the present model puts forward a robust physical mechanism for the shaping of the ice in the bottom part of the convection cell.

Next, we perform systematical numerical simulations to explore how  $\beta$  affects the extent and morphology of the ice front, with  $0 \leq \beta \leq 180$  (with the coordinate system attached to the cell). We limit our study to  $T_b = 10^\circ\text{C}$ , but the results are easy to be generalized to other situations.

First, we calculate the heat transfer rate, which when expressed dimensionlessly is the global Nusselt number [Fig. 3(a)],  $\text{Nu} = (\langle u_y T \rangle - \kappa \partial_y \langle T \rangle) / (\kappa \Delta T / H)$ , where  $\langle \dots \rangle$  represents an average over time and the whole cell volume, and  $H$  is the system height. It is noteworthy that there is convection both at  $\beta = 0$  (heating from below) and  $\beta = 180$  (heating from above). Remarkably, when  $\beta = 180$ , the fluid is unstably stratified in the temperature interval between  $T_0$  and  $T_c$  which accounts for creating the convection. The latter feature is specific to water and does not occur in other systems with the working fluid's density increasing with temperature. Figures 3(b)–3(h) show the temperature field with different  $\beta$  from simulations (for more results, see the Supplemental Material [38]). The inclination results in different levels of thermal stratification, which induces huge modifications to the ice front morphology. When  $\beta = 0$ , there is a stably stratified layer (from  $T_0$  to  $T_c$ ) on top of the unstably stratified layer (from  $T_c$  to  $T_b$ ). As the cell is tilted with a small  $\beta$ , the convection is strong enough to squeeze the stably stratified layer to be closely attached to the ice front, so the ice morphology is influenced by a single-roll convective flow [see Figs. 3(b) and 3(c)]. As  $\beta$  increases towards  $90$ , the inclination of the temperature gradient with respect to the gravity is strong enough to break down the stratification and thus the stably stratified layer is set into motion in the form of a clockwise convective roll (an upward cold water current) which competes with the initially anticlockwise roll (downward warm water current). The shielding effect is prominent because the ice thickness reaches a local maximum, and the hot plumes impacting on the top part of the ice induce a local minimum of the ice thickness, so based on these two kinds of effects, the ice front presents an inflection point during the transition from the thickest to the thinnest part, which has also been reported in Figs. 1(b) and 1(c). The flow motion of the original stably stratified layer intensifies as  $\beta$  increases for  $\beta < 90$ . Beyond  $\beta = 90$ , the stratification configuration flips over. On the whole, the intensity of convection is higher at  $0 < \beta < 90$  than that of  $90 < \beta < 180$ . This is to be connected to the different thermal differences across the respective unstably stratified layers which are  $(T_c - T_0) \approx 4 \text{ K}$  in the former and  $(T_b - T_c) \approx 6 \text{ K}$  in the latter case. This change in driving strength also accounts for the observed results of  $\text{Nu}$  [Fig. 3(a)].

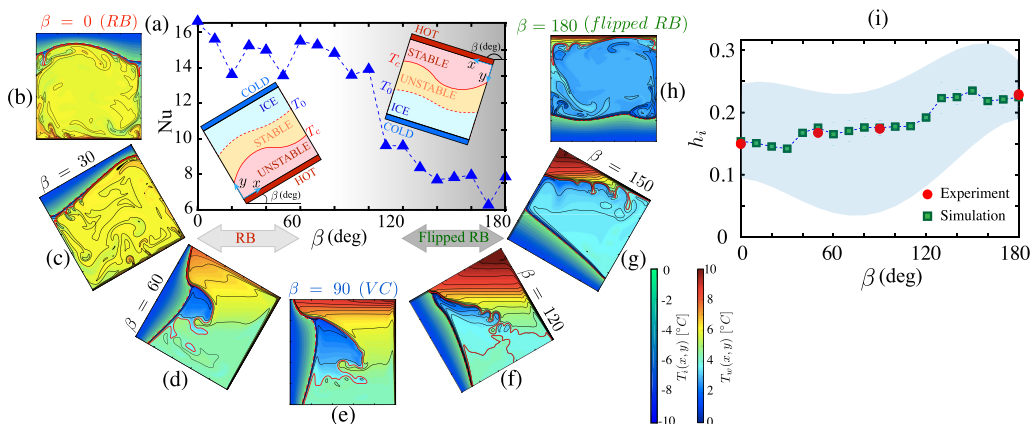


FIG. 3. (a) Nu as a function of  $\beta$ . Insets: Sketches of the arrangement of stably and unstably stratified layers of the RB regime,  $\beta < 90$  (left), and flipped RB,  $\beta > 90$  (right). Error bars (estimated based on the temporal time series of Nu in one simulation) are smaller than the symbols. The way to measure the systematic error (i.e., ensemble average, qualitatively reflected by the scatter of the data) is to perform multiple and independent simulations, which is numerically expensive and therefore is not considered here. (b)–(h) Instantaneous temperature field in ice,  $T_i(x, y)$ , and water,  $T_w(x, y)$ , and isotherms (black thin lines) at the equilibrium state for different angles  $\beta = [0, 180]$ . The red dashed line and red thick line in (b)–(h) are 0 and  $4^\circ\text{C}$  isotherms, respectively. (i) Global ice thickness  $h_i$  as a function of  $\beta$ . The shaded area shows the spatial variation of  $h_i(x)$  in the simulations. The parameters are  $T_b = 10^\circ\text{C}$  and  $T_t = -10^\circ\text{C}$  for all cases.

To account for the influence of  $\beta$  in a quantitative way, we now calculate the stationary global ice thickness ratio,  $h_i = \langle h_i(x, y) \rangle_{x,t}$ , where  $\langle \cdot \cdot \rangle_{x,t}$  represents an average over time and  $x$ -axis direction. Figure 3(i) reports  $h_i$ , as a function of  $\beta$ .  $h_i$  shows an increasing trend as  $\beta$  increases because the heat transfers less efficiently for large  $\beta$  (i.e., flipped RB system). The results from experiments (red circles) and simulations (green squares) agree well with each other. It is noteworthy that the ice front is highly variable in space as a result of the different coupling with turbulent flow structures. Here, the spatial fluctuations of the ice thickness are represented by the local maximum and minimum of  $h_i$ , which is highlighted by the shaded area.

Coming back to cases when  $\beta$  is around 90, we can observe a peculiar yet robust form of ice front morphology (which can be observed in the range of  $\beta = 40$ – $140$ ). In fact, the aforementioned boundary-layer model can be extended to the tilted system, by modifying  $C_1$ , with  $C_1 = \{g_x[1 - \rho(T_m)/\rho_c] - g_y\mathcal{H}[\beta - 90^\circ][1 - \rho(T_0)/\rho_c]\}/(\nu\kappa)^{1/4}$ , where  $\mathcal{H}$  is the Heaviside step function,  $g_x = g \sin \beta$ ,  $g_y = g \cos \beta$ . The first term in  $C_1$  results from the inclination effect, and the second part originates from the inherent buoyancy contribution induced by the density difference, and is present only for inclinations larger than  $90^\circ$ . Figures 4(c)–4(m) show the comparison of the ice front morphology between simulations (shaded area) and model prediction (dashed line). As shown, the model can qualitatively capture behaviors of the ice front at the inception of the thermal boundary. Note when  $\beta < 40$  and  $\beta > 140$ , the boundary layer attached to the ice front is disturbed because of the plume impacting under intensive interactions of the stably and unstably stratified layers, so the model cannot be utilized. A second limitation of the model is that the adopted expression for  $\delta_T(S)$  is based on VC [47] but it does not involve possible dependencies on the cell inclination. Nevertheless, it is remarkable that the model already performs well in a wide range of  $\beta$ . Further studies are needed to improve or quantitatively refine the model.

Another feature of the ice front is the position  $\Delta x_0$  where  $h_i(x)$  reaches maximum [symbols in Fig. 4(b)]. As discussed before, the local maximum of  $h_i$  originates from the competition of the buoyancy intensity between two counter-rotating rolls. The buoyancy intensity of the cold

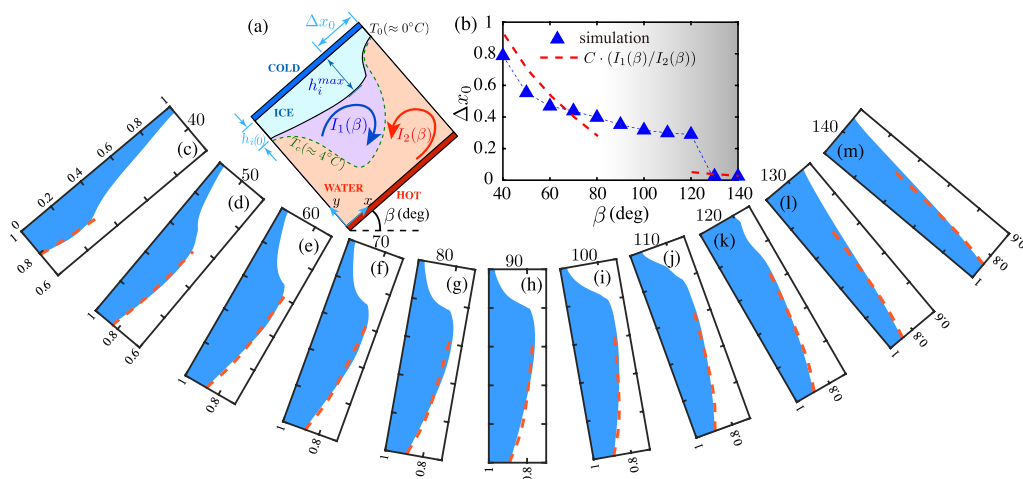


FIG. 4. (a) Sketch of the buoyancy-intensity model to explain the position of the maximum ice thickness. The buoyancy intensities of the clockwise and anticlockwise convective rolls are  $I_1(\beta)$  and  $I_2(\beta)$ , respectively.  $\Delta x_0$  locates the position of the maximum of the  $h_i(x)$ , which is dimensionless normalized by  $H$ .  $h_i(0)$ , an input parameter of the boundary-layer model, is roughly constant and around  $h_i$ .  $h_i(0)$  vs  $\beta$  is reported in the Supplemental Material [38]. (b)  $\Delta x_0$  as a function of  $\beta$  and its comparison with model predictions (adjustable constant  $C = 0.08$ ). (c)–(m) Comparison of the ice front morphology between simulations (shaded area) and the model (dashed line) under different  $\beta$  near  $90^\circ$ .

(clockwise) roll [blue arrow in Fig. 4(a)],  $I_1(\beta)$ , and of the warm (anticlockwise) roll [red arrow in Fig. 4(a)],  $I_2(\beta)$ , can be approximately evaluated with

$$\begin{aligned} I_1(\beta) &= g_x \left( 1 - \frac{\rho(T_m)}{\rho_c} \right) - g_y \mathcal{H}[\beta - 90^\circ] \left( 1 - \frac{\rho(T_0)}{\rho_c} \right), \\ I_2(\beta) &= g_x \left( 1 - \frac{\rho(T_{m2})}{\rho_c} \right) + g_y \mathcal{H}[90^\circ - \beta] \left( 1 - \frac{\rho(T_b)}{\rho_c} \right), \end{aligned} \quad (2)$$

where the mean temperature  $T_m = (T_0 + T_c)/2$  and  $T_{m2} = (T_b + T_c)/2$ . Equation (2) holds when  $\beta \neq 90^\circ$  (for details, see the Supplemental Material [38]). The intensity ratio  $[I_1(\beta)/I_2(\beta)]$  captures the trend of  $\Delta x_0$  as a function of  $\beta$ , at least for  $10 < |\beta - 90| < 50$ . A quantitative agreement is obtained by an adjustment multiplicative factor  $C \simeq 0.08$  [red dashed line in Fig. 4(b)]. This heuristic model provides further evidence that the competition of two convective rolls accounts for the form of ice morphology.

To summarize, we found that the existence of a cold upward convective current, due to the density anomaly of water, accounts for the ice shaping in a convective cell. We provide a physical understanding of the main features of the ice morphology in a wide range of system inclinations. The present exploration offers deeper insight into comprehending the liquid-solid interface morphology induced by the coupling between phase transitions and natural convection with possible applications in geophysical and climate sciences.

This work was supported by Natural Science Foundation of China under Grants No. 11988102, No. 91852202, and No. 11861131005.

[1] P. Meakin and B. Jamtveit, Geological pattern formation by growth and dissolution in aqueous systems, *Proc. R. Soc. A* **466**, 659 (2010).

- [2] T. Alboussiere, R. Deguen, and M. Melzani, Melting-induced stratification above the Earth's inner core due to convective translation, *Nature (London)* **466**, 744 (2010).
- [3] M. Epstein and F. Cheung, Complex freezing-melting interfaces in fluid flow, *Annu. Rev. Fluid Mech.* **15**, 293 (1983).
- [4] M. G. Worster, Convection in mushy layers, *Annu. Rev. Fluid Mech.* **29**, 91 (1997).
- [5] A. Scagliarini, E. Calzavarini, D. Mansutti, and F. Toschi, Modelling sea ice and melt ponds evolution: Sensitivity to microscale heat transfer mechanisms, in *Mathematical Approach to Climate Change and its Impacts* (Springer, Berlin, 2020), pp. 179–198.
- [6] H. E. Huppert and J. S. Turner, On melting icebergs, *Nature (London)* **271**, 46 (1978).
- [7] D. Russell-Head, The melting of free-drifting icebergs, *Ann. Glaciol.* **1**, 119 (1980).
- [8] E. Rignot, S. Jacobs, J. Mouginot, and B. Scheuchl, Ice-shelf melting around Antarctica, *Science* **341**, 266 (2013).
- [9] N. Kousha, M. Hosseini, M. Aligoodarz, R. Pakrouh, and R. Bahrampoury, Effect of inclination angle on the performance of a shell and tube heat storage unit—an experimental study, *Appl. Therm. Eng.* **112**, 1497 (2017).
- [10] A. V. Pogorelova, V. L. Zemlyak, and V. M. Kozin, Moving of a submarine under an ice cover in fluid of finite depth, *J. Hydrodyn.* **31**, 562 (2019).
- [11] E. W. Hester, C. D. McConnochie, C. Cenedese, L.-A. Couston, and G. Vasil, Aspect ratio affects iceberg melting, *Phys. Rev. Fluids* **6**, 023802 (2021).
- [12] J. Malm, Bottom buoyancy layer in an ice-covered lake, *Water Resour. Res.* **34**, 2981 (1998).
- [13] T. A. Kowalewski and M. Rebow, Freezing of water in a differentially heated cubic cavity, *Int. J. Comput. Fluid. D* **11**, 193 (1999).
- [14] G. Veronis, Penetrative convection, *Astrophys. J.* **137**, 641 (1963).
- [15] A. Arid, T. Kouskou, S. Jegadheeswaran, A. Jamil, and Y. Zeraouli, Numerical simulation of ice melting near the density inversion point under periodic thermal boundary conditions, *Fluid Dyn. Mater. Process.* **8**, 257 (2012).
- [16] E. Large and C. Andereck, Penetrative Rayleigh-Bénard convection in water near its maximum density point, *Phys. Fluids* **26**, 094101 (2014).
- [17] M. Corcione and A. Quintino, Penetrative convection of water in cavities cooled from below, *Comput. Fluids.* **123**, 1 (2015).
- [18] A. Badarch and H. Tokuzo, Phase change simulations of water near its density inversion point by lattice Boltzmann method, in *Proceedings of the 23rd IAHR International Symposium on ice* (2016), IAHR ID No. 18423, pp. 1–8.
- [19] P. Léard, B. Favier, P. Le Gal, and M. Le Bars, Coupled convection and internal gravity waves excited in water around its density maximum at 4 °C, *Phys. Rev. Fluids* **5**, 024801 (2020).
- [20] D. Lecoanet, M. Le Bars, K. J. Burns, G. M. Vasil, B. P. Brown, E. Quataert, and J. S. Oishi, Numerical simulations of internal wave generation by convection in water, *Phys. Rev. E* **91**, 063016 (2015).
- [21] S. Toppaladoddi and J. S. Wettlaufer, Penetrative convection at high Rayleigh numbers, *Phys. Rev. Fluids* **3**, 043501 (2018).
- [22] C. Dietsche and U. Müller, Influence of Bénard convection on solid-liquid interfaces, *J. Fluid Mech.* **161**, 249 (1985).
- [23] Y. Hu, D. Li, S. Shu, and X. Niu, Lattice Boltzmann simulation for three-dimensional natural convection with solid-liquid phase change, *Int. J. Heat Mass Transfer* **113**, 1168 (2017).
- [24] H. Inaba and T. Fukuda, Natural convection in an inclined square cavity in regions of density inversion of water, *J. Fluid Mech.* **142**, 363 (1984).
- [25] A. Quintino, E. Ricci, S. Grignaffini, and M. Corcione, Heat transfer correlations for natural convection in inclined enclosures filled with water around its density-inversion point, *Int. J. Therm. Sci.* **116**, 310 (2017).
- [26] A. Quintino, E. Ricci, S. Grignaffini, and M. Corcione, Optimal inclination for maximum convection heat transfer in differentially-heated enclosures filled with water near 4 °C, *Heat Transfer Eng.* **39**, 499 (2018).

- [27] B. Kamkari, H. Shokouhmand, and F. Bruno, Experimental investigation of the effect of inclination angle on convection-driven melting of phase change material in a rectangular enclosure, *Int. J. Heat Mass Transfer* **72**, 186 (2014).
- [28] B. Kamkari and H. J. Amlashi, Numerical simulation and experimental verification of constrained melting of phase change material in inclined rectangular enclosures, *Int. Commun. Heat Mass Transfer* **88**, 211 (2017).
- [29] L. Zeng, J. Lu, Y. Li, W. Li, S. Liu, and J. Zhu, Numerical study of the influences of geometry orientation on phase change material's melting process, *Adv. Mech. Eng.* **9**, 1 (2017).
- [30] S. Madruga and J. Curbelo, Effect of the inclination angle on the transient melting dynamics and heat transfer of a phase change material, *Phys. Fluids* **33**, 055110 (2021).
- [31] Z. Wang, E. Calzavarini, C. Sun, and F. Toschi, How the growth of ice depends on the fluid dynamics underneath, *Proc. Natl. Acad. Sci. USA* **118**, e2012870118 (2021).
- [32] E. D. Siggia, High Rayleigh number convection, *Annu. Rev. Fluid Mech.* **26**, 137 (1994).
- [33] E. Bodenschatz, W. Pesch, and G. Ahlers, Recent developments in Rayleigh-Bénard convection, *Annu. Rev. Fluid Mech.* **32**, 709 (2000).
- [34] G. Ahlers, S. Grossmann, and D. Lohse, Heat transfer and large scale dynamics in turbulent Rayleigh-Bénard convection, *Rev. Mod. Phys.* **81**, 503 (2009).
- [35] D. Lohse and K.-Q. Xia, Small-scale properties of turbulent Rayleigh-Bénard convection, *Annu. Rev. Fluid Mech.* **42**, 335 (2010).
- [36] F. Chillà and J. Schumacher, New perspectives in turbulent Rayleigh-Bénard convection, *Eur. Phys. J. E* **35**, 58 (2012).
- [37] E. Calzavarini, Eulerian-Lagrangian fluid dynamics platform: The CH4-PROJECT, *Software Impacts* **1**, 100002 (2019).
- [38] See Supplemental Material at <http://link.aps.org/supplemental/10.1103/PhysRevFluids.6.L091501> for the introduction of experimental and numerical methods, systematic investigation of various inclination angles, the boundary layer model, and the buoyancy-intensity model.
- [39] S. Succi, *The Lattice-Boltzmann Equation: For Fluid Dynamics and Beyond* (Oxford University Press, Oxford, UK, 2001).
- [40] C. Huber, A. Parmigiani, B. Chopard, M. Manga, and O. Bachmann, Lattice-Boltzmann model for melting with natural convection, *Int. J. Heat Fluid Flow* **29**, 1469 (2008).
- [41] B. Rabbanipour Esfahani, S. C. Hirata, S. Berti, and E. Calzavarini, Basal melting driven by turbulent thermal convection, *Phys. Rev. Fluids* **3**, 053501 (2018).
- [42] S. Chen, Y. Y. Yan, and W. Gong, A simple lattice Boltzmann model for conjugate heat transfer research, *Int. J. Heat Mass Transfer* **107**, 862 (2017).
- [43] M. Faden, A. Knig-Haagen, and D. Bruggemann, An optimum enthalpy approach for melting and solidification with volume change, *Energies* **12**, 868 (2019).
- [44] B. Gebhart and J. C. Mollendorf, A new density relation for pure and saline water, *Deep Sea Res.* **24**, 831 (1977).
- [45] J. Dash, A. Rempel, and J. Wettlaufer, The physics of premelted ice and its geophysical consequences, *Rev. Mod. Phys.* **78**, 695 (2006).
- [46] C. Sun, Y.-H. Cheung, and K.-Q. Xia, Experimental studies of the viscous boundary layer properties in turbulent Rayleigh-Bénard convection, *J. Fluid Mech.* **605**, 79 (2008).
- [47] A. Bejan, *Convection Heat Transfer* (Wiley, Hoboken, NJ, 2013).
- [48] F. M. White and I. Corfield, *Viscous Fluid Flow*, Vol. 3 (McGraw-Hill, New York, 2006).
- [49] O. Shishkina, Momentum and heat transport scalings in laminar vertical convection, *Phys. Rev. E* **93**, 051102(R) (2016).